




# Fast Ion Conduction of Sintered Glass-Ceramic Lithium Ion Conductors Investigated by Impedance Spectroscopy and Coaxial Reflection Technique

R. F. Samsinger,<sup>1,2,z</sup>  M. Letz,<sup>2</sup> J. Schuhmacher,<sup>2</sup> M. Schneider,<sup>2</sup> A. Roters,<sup>2</sup> D. Kienmund,<sup>3</sup> H. Maune,<sup>3</sup> and A. Kwade<sup>1</sup>

<sup>1</sup>Institute for Particle Technology, TU Braunschweig, 38104 Braunschweig, Germany

<sup>2</sup>SCHOTT AG, Research and Development, 55122 Mainz, Germany

<sup>3</sup>Institute of Microwave Engineering, TU Darmstadt, 64295 Darmstadt, Germany

As the ionic conductivity of solid-state lithium ion conductors rises, knowledge of the detailed conductivity mechanisms is harder to obtain due to the limited frequency resolution of the traditional impedance spectrometers. Moreover, the data is easily affected by the local microstructure (i.e. pores, grain-boundaries) and the preparation conditions. The aim of this work is to demonstrate the feasibility of the coaxial reflection technique as a reliable tool to study fast ionic conductors (i.e.  $\sigma > 10^{-4} \text{ S cm}^{-1}$ ). Especially the relative permittivity can be determined more accurately at room temperature. For the first time the electrical performance of LATP and LLZO manufactured via a scalable top-down glass-ceramic route is evaluated. The density turns out to be a key parameter influencing both relative permittivity and resulting conductivities. For a 100% dense LATP sample the coaxial reflection technique reveals a high grain-core conductivity of  $6 \times 10^{-3} \text{ S cm}^{-1}$  similar to the conductivity of ideal single crystals.

© 2020 The Author(s). Published on behalf of The Electrochemical Society by IOP Publishing Limited. This is an open access article distributed under the terms of the Creative Commons Attribution 4.0 License (<http://creativecommons.org/licenses/by/4.0/>), which permits unrestricted reuse of the work in any medium, provided the original work is properly cited. [DOI: [10.1149/1945-7111/abc0a9](https://doi.org/10.1149/1945-7111/abc0a9)]



Manuscript submitted June 17, 2020; revised manuscript received September 30, 2020. Published October 21, 2020.

Supplementary material for this article is available [online](#)

Since the last decades, several new solid lithium ion conductors reached the targeted conductivity of  $10^{-3} \text{ S cm}^{-1}$  to be competitive with classical liquid electrolytes.<sup>1,2</sup> Prominent examples are Garnet-type ( $\text{Li}_{6.4}\text{La}_3\text{Zr}_{1.4}\text{Ta}_{0.6}\text{O}_{12}$ , LLZO),<sup>3</sup> NASICON-type ( $\text{Li}_{1.3}\text{Al}_{0.3}\text{Ti}_{1.7}\text{P}_3\text{O}_{12}$ , LATP),<sup>4</sup> Argryrodite-type ( $\text{Li}_6\text{PS}_5\text{Cl}_{0.5}\text{Br}_{0.5}$ ),<sup>5</sup> and thio-LISICON-type ( $\text{Li}_{10}\text{GeP}_2\text{S}_{12}$ ).<sup>6</sup> More recently  $\text{Li}_{9.54}\text{Si}_{1.74}\text{P}_{1.44}\text{S}_{11.7}\text{Cl}_{0.3}$ <sup>7</sup> and advanced Li-rich antiperovskite-type electrolytes<sup>8,9</sup> have been discovered with a conductivity  $>10^{-2} \text{ S cm}^{-1}$ . For further optimization of these electrolytes, detailed knowledge about the conduction mechanism is necessary. This is usually achieved by Electrochemical Impedance Spectroscopy (EIS) and Nuclear Magnetic Resonance (NMR). Both methods have high accuracy and are well established in academic world and industry. However, for fast lithium ion conductors, these methods more often encounter their limits.

For example, LATP is known to have high grain-core conductivity, but high resistance pathways across grain-boundaries. State of the art EIS measurements setups are capable to measure up to several MHz. At room temperature, the grain-core conductivity of LATP is too high to be well resolved. Therefore, one has to measure below room temperature to detect both the grain-core and grain-boundary process (or even more processes) and extrapolate via the Arrhenius law.<sup>10,11</sup> Alternatively, one has to change sample geometry (i.e. enlarging crystals and decrease the electrode area). This method often leads to experimental challenges. Furthermore, micro-electrodes lead to good estimations for single crystals, but still with an uncertainty of up to 10%.<sup>4</sup>

Via NMR different processes can be detected straightforwardly. Several timescales are available probing nearest neighbor interactions up to diffusion-lengths in the micron regime. However, a main disadvantage is conversion from NMR diffusion coefficients to the industrial more relevant conductivity. This is regularly done via the Nernst-Einstein equation, which strictly only applies for conductors with non-interacting charge carriers.<sup>12</sup> Although this is the case for dilute liquid solutions, deviations will occur for solid ion conductors. Additionally, the average jump distance is a crucial parameter. Yet, experimental estimation might be a significant error source. A further disadvantage is that calculated activation energies typically

differ from the ones obtained from EIS measurements. This is explained with the restricted motion on shorter time scales in NMR experiments<sup>13</sup> and may also arise as a consequence of the temperature dependent broadening of the distribution of correlation times.<sup>14</sup> Hence, it is rather a coincidence if the estimated conductivity via the Nernst-Einstein equation perfectly matches the real conductivity at room temperature.

In this study, we want to highlight the extension of the measurement range of EIS from MHz to GHz as a reliable tool to study conductivity mechanisms and dielectric properties of fast lithium ion conductors. In the past, this has only been done occasionally with fast lithium ion conductors<sup>15,16</sup> or with slow room temperature lithium ion conductors, which are measured at higher temperatures.<sup>17,18</sup> To prove the feasibility of the method, two glass-ceramic LATP powders, and one glass-ceramic LLZO powder were sintered and measured via classical EIS and a coaxial reflection technique (CRT). In contrast to previous studies, these powders were obtained from a unique melting route at semi-industrial scale. Thus, inhomogeneity effects of different batches<sup>15</sup> are less pronounced. Furthermore, we demonstrate that amorphous phase assisted sintering with the intrinsic amorphous phase of the glass-ceramic powders is a successful strategy to obtain dense samples with very high conductivity.

## Experimental

**Sample preparation.**—The glass-ceramic lithium ion conductors  $\text{Li}_{1.3}\text{Al}_{0.3}\text{Ti}_{1.7}\text{P}_3\text{O}_{12}$  (LATP) and  $\text{Li}_7\text{La}_3\text{Zr}_2\text{O}_{12}$  (LLZO)<sup>a</sup> were produced via advanced melting routes at the SCHOTT AG.<sup>19,20</sup> A schematic comparison with state-of-the-art solid-state reaction and sol-gel processes is given in Fig. S1 (available online at [stacks.iop.org/JES/167/140510/mmedia](https://stacks.iop.org/JES/167/140510/mmedia)) as illustration. As glass-ceramics, these ion conductors consist of both a ceramic and an unique amorphous phase. Thus, the conduction mechanism may vary from the pure ceramic LLZO/LATP samples in literature. Two different LATP powders with the same crystalline stoichiometry, but different content of amorphous phase are investigated. In addition, the conduction mechanism is compared to a LLZO sample. LLZO has the disadvantage that the high conductive cubic modification has to be stabilized at room temperature. Therefore, changing the amount

<sup>z</sup>E-mail: [r.samsinger@tu-braunschweig.de](mailto:r.samsinger@tu-braunschweig.de)

<sup>a</sup>The exact composition is proprietary.

of amorphous phase without disturbing the stability of the cubic phase is challenging and comparison of different LLZO powders will be a subject in future.

Compared to pure ceramic LTP and LLZO, the skeleton density of glass-ceramic LTP and LLZO is reduced, due to the lower density of the amorphous phase. The LTP with low amorphous phase content will be denoted as LTP1. It has a skeleton density of  $2.86 \text{ g cm}^{-3}$ , which is close to the pure ceramic density of  $2.90 \text{ g cm}^{-3}$ . The second LTP with high amorphous phase content has a skeleton density of  $2.80 \text{ g cm}^{-3}$  and will be called LTP2. The difference in density is more significant for glass-ceramic LLZO with  $4.84 \text{ g cm}^{-3}$  compared to the ideal density of  $5.10 \text{ g cm}^{-3}$ .

Amongst all powders, the volume based median particle size is  $1 \mu\text{m}$  or below. The particle size distributions are rather narrow. The powders were pressed to discs with a diameter of 10 mm, and a thickness of 1 to 2 mm. Afterwards the discs were sintered as described elsewhere.<sup>19,21</sup> Finally, the sintered discs were transferred into an argon-filled glove box and polished with #360 up to #400 SiC sandpaper.

**Measurement techniques.**—Prior to the measurements the samples have been sputtered with gold to ensure sufficient electric contact. Classical EIS has been performed with a Novocontrol Alpha-A-Analyzer in combination with a ZGS Active Sample Cell Test Interface at SCHOTT. The voltage amplitude was set to 20 mV. The frequency range was set from 0.1 Hz until 20 MHz. A sealed measurement cell was used to avoid contact of the LLZO with air. ZView2 (Scribner Associates Inc.) was used for fitting. Afterwards the samples were sealed into alumina pouch-bags and transferred to the IMP of TU Darmstadt for further characterization. At the IMP a Keysight E4991B Impedance Analyzer in the frequency range of 1 MHz to 3 GHz was used for the reflection measurement of the dielectric halfspace with an open-ended probe (i.e. skin depth  $\gg$  thickness of the probe)<sup>b</sup>. A detailed introduction can be found in the publication of Bömer et al.<sup>22</sup> The measurement setup contains a sample fixture made from an APC-7 connector.<sup>23</sup> Note that the thickness of the gold layers is about 100 nm, while the skin-depth for gold at these high frequencies is still several microns. As ion-conductors, in contrast to low-loss dielectric ceramics, have a higher dielectric-loss (i.e. due to the desired ionic motion), the additional dielectric-loss in the gold-layers does not deteriorate the results. At frequencies between 1 GHz and 3 GHz, a series inductance will dominate the measurement due to the metallic connections. However, at room temperature the frequency range above 1 GHz is yet of no interest. Thus, for evaluation, the highest frequencies containing no sample information, were neglected. All measurements were performed in air. Nevertheless, the correct bulk conductivity can always be determined, even if LLZO slightly reacts with condensed water and carbon dioxide. During the short measurement time, the reactions can only take place at the surface. Thus, the bulk properties are unaffected. Note that for long term studies the measurement setup should be transferred into an argon-filled glove box.

## Results and Discussion

**Structural analysis.**—For high conductivity, the purity of the ceramic phase content of LTP and LLZO is crucial. For example, LTP easily forms  $\text{AlPO}_4$  (JCPDS: 00-011-0500) enriched phases at grain-boundaries or unwanted  $\text{TiO}_2$  (JCPDS: 00-088-1175, 00-084-1286) impurity phases.<sup>24</sup> LLZO samples are even more sensitive. Besides the tetragonal LLZO phase,  $\text{La}_2\text{Zr}_3\text{O}_7$  (JCPDS: 01-075-03446) and  $\text{Li}_2\text{CO}_3$  (JCPDS: 01-083-1454) are well-known insulating impurity phases. The XRD of glass-ceramic LTP1, LTP2, and LLZO is shown in Fig. 1.

Only the LTP phase and the cubic LLZO phase can be detected, without any additional impurities. Consequently, a high conductivity can be expected. Furthermore, for the LTP1 and LTP2 the effect of the different amorphous phase content can be investigated without perturbations from impurities.

**Morphological analysis.**—A necessary pre-condition for a high conductivity is a high density of the samples. As mentioned before, the skeleton density of the glass-ceramic LTP and LLZO particles is lower compared to the theoretical density of pure ceramic LTP and LLZO. To calculate the relative density of the cylindrical pellets, the density obtained from the weight and geometrical dimensions is divided by the skeleton density of each glass-ceramic electrolyte.

The open porosity of pressed pellets is about 34%. However, after sintering LTP1 samples still have a low geometrical density (solids concentration) of about 66% to 70%. In contrast, the LTP2 samples expose an enormous shrinkage leading to very dense cross-section with nearly no pores. Also for the LLZO samples the amorphous phase leads to high densities of 95% to 97%. The huge advantage of amorphous phase assisted sintering is best revealed via SEM images. In Fig. 2 the cross-sections of a LTP1 and a LTP2 sample are shown. For LTP1 only slight neck growth is visible, while LTP2 has a dense structure with well-connected coarsened particles. In addition, the dense structure of LLZO is revealed in Fig. S2. For pure ceramic electrolytes highest relative densities of more than 98% are usually achieved by hot-pressing.<sup>16,25</sup> Although the glass-ceramic LLZO has not reached such a high density yet, the LTP2 sample demonstrates that such a high relative density could also be achieved via amorphous phase assisted sintering. A pressure-free sintering is very attractive for continuous industrial processes (e.g. tape-casting). In addition, the measurement results can be easily compared with each other during the up-scaling process.

**Electrochemical performance.**—The combined normalized impedance data obtained from the classical EIS measurement with the Novo-control Alpha-A analyzer and the high-frequency CRT measurement with the Keysight E4991B is shown in Fig. 3. The impedance has been normalized with respect to the area and thickness of the samples for comparison, due to the different shrinkage.

At low frequencies the blocking of lithium ions at the gold electrode is visible. This leads to a straight line of constant slope. A deviation from  $90^\circ$  vs the abscissa  $Z'$  can be interpreted as an effect from a rough electrode surface with microscopic inhomogeneities. Another possible origin might be an alloying of lithium from the electrolytes with the gold electrodes.

For the LTP1 and LTP2 samples, the classical EIS resolves a depressed semicircle, i. e. a resistor in parallel with a constant-phase-element (CPE), at intermediate frequencies (black squares/blue triangles). According to Brug et al.<sup>26</sup> the fractional value of a CPE (with fit parameters  $Q$  and  $\alpha$ ) in parallel to a resistor  $R$  can be related to a physical meaningful capacitance.

$$C = Q \frac{1}{\alpha} \cdot R^{\frac{1-\alpha}{\alpha}} \quad [1]$$

The obtained capacities at intermediate frequencies are in the order of  $10^{-9}$  F. According to Irvine et al.<sup>27</sup> capacities in the nF-regime can be interpreted as a grain-boundary process. The alpha factors lie within the range of 0.79–0.90 in agreement with typical values for ceramic LLZO/LTP.<sup>28,29</sup>

At high frequencies, the resistance from origin indicates another process. It is rather difficult to fit this process with another semicircle accurately.

In contrast, the CRT is capable to resolve this semi-circle at room temperature. For LTP1 there is a very small deviation of the impedance compared to the EIS-data. Due to experimental limitations, the thickness and diameter of this sample are at the upper limit that is acceptable for the metallic fixture of the sample holder. The metallic fixture may partially remove the sputtered gold layer during

<sup>b</sup>In known literature, there are several terms and modifications of this measurement technique. Therefore, we prefer the more general term coaxial reflection technique (CRT).

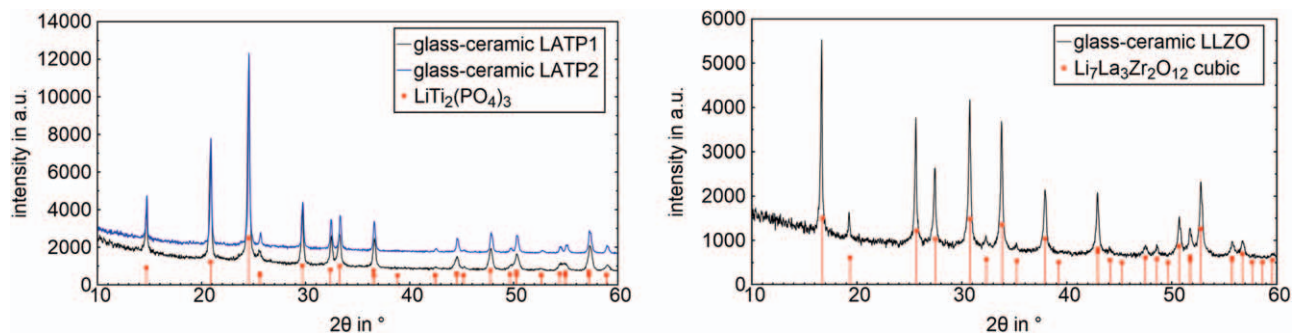


**Figure 1.** (a) XRD of glass-ceramic LAMP particles. (b) XRD of glass-ceramic LLZO particles.

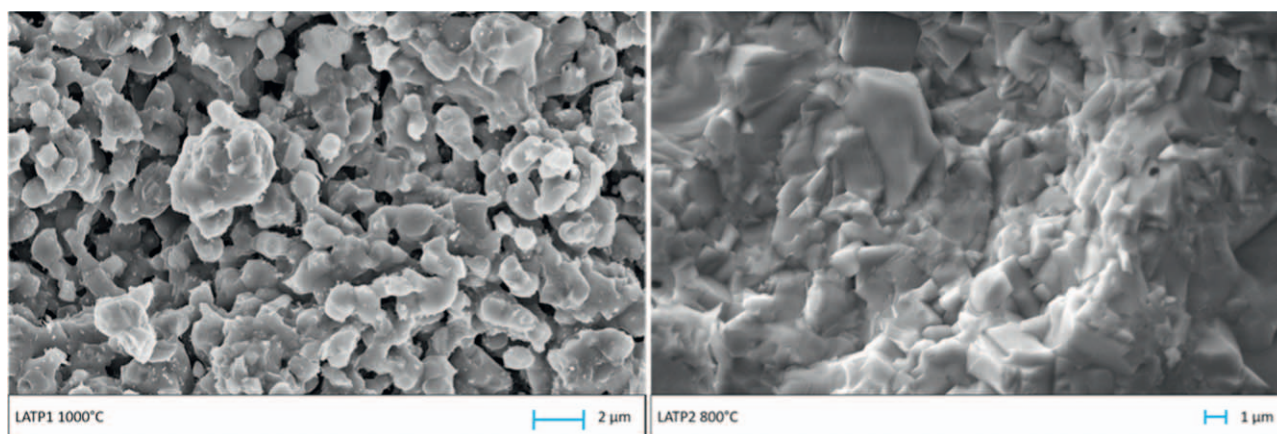


**Figure 2.** (a) Cross-section of LAMP1 with necks between particles and high residual porosity. (b) Cross-section of LAMP2. The higher content of amorphous phase leads to a significant densification.

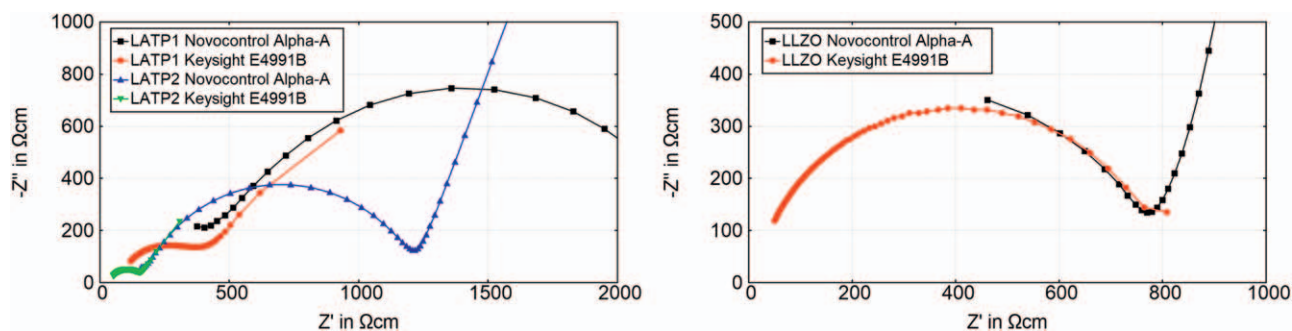


**Figure 3.** (a) Nyquist-diagram of Au-LAMP-Au with normalized complex impedance  $Z$ . Within the classical measurement range, the grain-core process of LAMP1 and LAMP2 can only be estimated. (b) Nyquist-diagram of Au-LLZO-Au with normalized complex impedance  $Z$ . Only one bulk semi-circle can be detected at highest frequencies.

sample installation, leading to a lower effective contact area. Nevertheless, the grain-core<sup>c</sup> semi-circle is well resolved. In agreement with Irvine et al. the capacity is in the order of  $10^{-11}$  F.

The effective conductivity of the sintered discs can be calculated according to Eq. 2:

$$\sigma = \frac{1}{R} \cdot \frac{t}{A} \quad [2]$$

Where  $R$  is the fitted resistance,  $t$  is the thickness of the sample, and  $A$  is the electrode area. For LAMP1 the grain-boundary conductivity from EIS is  $5.04 \times 10^{-4} \text{ S cm}^{-1}$  with a grain-core conductivity of  $2.37 \times 10^{-3} \text{ S cm}^{-1}$ . The grain-core conductivity obtained from the

CRT is  $2.15 \times 10^{-3} \text{ S cm}^{-1}$ . The LAMP2 has a grain-boundary conductivity of  $9.49 \times 10^{-4} \text{ S cm}^{-1}$  and a very high grain-core conductivity of  $6.00 \times 10^{-3} \text{ S cm}^{-1}$ , which matches well with the one obtained from the CRT setup of  $5.91 \times 10^{-3} \text{ S cm}^{-1}$ . Therefore, both grain-core and grain-boundary conductivity increase with density. This corresponds well to the findings of Wang et al.<sup>10</sup> who measured a grain-core conductivity of  $6.50 \times 10^{-3} \text{ S cm}^{-1}$  for a 97% dense sample with comparable ceramic composition. However, their grain-boundary conductivity is considerably lower ( $2.7 \times 10^{-5} \text{ S cm}^{-1}$ ). A possible explanation might be the enormous grain-growth (up to  $40 \mu\text{m}$ ) in the absence of a suitable amorphous phase. Jackman and Cutler<sup>30</sup> revealed that coarse-grained LAMP leads to increased microcracking at grain-boundaries and increased resistance. The maximum grain-boundary conductivity achieved for minimal cracking was  $7.2 \times 10^{-4} \text{ S cm}^{-1}$  with a relative density of 97%. This value is only a little lower than the grain-boundary

<sup>c</sup>The conduction within grains is herein denoted as “grain-core.” Sometimes, this is called “bulk,” especially when single-crystals are used or grain-core and grain-boundary contribution cannot be deconvoluted.

**Table I. Estimation of the relative permittivity according to Eq. 3.**

	Relative Permittivity from EIS	Relative Permittivity from CRT
LATP1	73.78	32.20
LATP2	106.17	76.83
LLZO	72.87	93.31

conductivity of LATP2. The SEM image of LATP2 demonstrates that liquid phase assistant sintering avoids abnormal grain-growth, which is consistent with this theory.

Additionally, the results of LATP2 can be compared to the glass-ceramic LLZO. Alike the amorphous phase leads to a high relative density. For LLZO in Fig. 3b only one semi-circle is visible even with the extension to the GHz regime. The capacity is in the order of  $10^{-11}$  F and can be identified with the bulk process. In literature<sup>31–33</sup> it is often assumed that a possible grain-boundary contribution is negligible and conductivity is taken from the intercept of the blocking-spike. Only few reports<sup>16,25</sup> of high conductive LLZO report a visible contribution from grain-boundaries. Especially, Tsai and et al.<sup>25</sup> observed an increased grain-boundary resistance at  $-30$  °C for samples with high grain sizes up to  $30$   $\mu\text{m}$  and thick grain-boundaries with impurity phases, while no grain-boundary semi-circle is present for a hot-pressed sample with grain sizes below  $10$   $\mu\text{m}$  and thinner grain-boundaries. Thus, at low temperatures where the relaxation time is sufficiently different from the grain-core process, these microstructure effects may explain the appearance of an additional semi-circle in the low-frequency range.

The conductivity of LLZO obtained from EIS is  $8.29 \times 10^{-4}$  S  $\text{cm}^{-1}$  and the one from the CRT is  $8.23 \times 10^{-4}$  S  $\text{cm}^{-1}$ . These values are within a similar order of magnitude compared to other LLZO with high relative density.

Regarding both measurement methods, obviously the resulting conductivity values are quite similar. However, for the EIS measurement one has to assume, that no other processes in the unresolved high-frequency regime are present.

The high-frequency relative permittivity (dielectric constant)  $\epsilon_r$  can be derived via Eq. 3

$$\epsilon_r = \frac{1}{i\omega\epsilon_0} \cdot \frac{1}{Z} \quad [3]$$

with the vacuum permittivity  $\epsilon_0 = 8.85419 \times 10^{-12}$  F  $\text{m}^{-1}$  and the imaginary unit  $i = \sqrt{-1}$ . As the normalized impedance  $Z$  can be fitted precisely, the limited frequency range of the EIS setup leads to an inaccurate high-frequency relative permittivity.

In contrast, via CRT the fast ionic transport processes are well resolved at room temperature. Hence, both conductivity and high-frequency relative permittivity can be determined precisely.

In Table I the calculated relative permittivities of the EIS and CRT are compared. The different relative permittivities of LATP1 and LATP2 samples might be explained with their microstructure.<sup>34</sup> Nevertheless, significant differences arise from the limited resolution of EIS. For example Rettenwander et al.<sup>35</sup> estimated the relative permittivity of several LLZO samples to be in the order of 40 to 60. Furthermore, the values were highly temperature-dependent. In agreement with the above discussion, they explained this effect via the limited frequency range of the EIS.

The correct estimation of the relative permittivity is particularly important for simulations. In a recent study de Klerk and Wagemaker<sup>36</sup> discussed the effect space-charge-layers in all-solid-state batteries. They used a relative permittivity of 15 for LATP and the value of 60 from Rettenwander et al.<sup>35</sup> Of course, our samples have different stoichiometry and an additional amorphous phase. Nevertheless, we emphasize to estimate the relative permittivity with the coaxial reflection technique using dense and homogenous samples. In addition, with NMR and other spectroscopic measurements a detailed knowledge of the electrochemical performance

could be achieved. Especially for the fast ion conductors described in the introduction, coaxial reflection technique might be very attractive.

## Conclusions

It was shown that the coaxial reflection technique is a feasible measurement tool expanding the measurement range of classical electrochemical impedance spectrometers. As a result, the ultra-fast conductivity processes at high frequencies could be resolved and interpreted, complementing first estimations from NMR or micro-electrode measurements. Furthermore, reliable high-frequency relative permittivities can be calculated at room temperature.

Besides chemical purity, the relative density of sintered samples is a key parameter for fast ionic conductivity. Sintering with the aid of an intrinsic amorphous phase proves to be an effective strategy to obtain electrolytes with advanced microstructure and a relative density of up to 100%. By optimizing the amorphous phase, glass-ceramic LATP has a high grain-boundary conductivity close to  $10^{-3}$  S  $\text{cm}^{-1}$ , which is among the best values for LATP measured so far. Moreover, the resolved grain-core conductivity of  $6 \times 10^{-3}$  S  $\text{cm}^{-1}$  matches well with the data known from single-crystals, demonstrating the feasibility of the coaxial reflection technique.

## Acknowledgments

Funding by the German Federal Ministry of Education and Research (Glanz, project number: 03X4623A; FELIZIA: 03XP0026D) is appreciated.

## ORCID

R. F. Samsinger  <https://orcid.org/0000-0003-2477-0686>

## References

1. K. Takada, *J. Power Sources*, **394**, 74 (2018).
2. B. Zhang, R. Tan, L. Yang, J. Zheng, K. Zhang, S. Mo, Z. Lin, and F. Pan, *Energy Storage Mater.*, **10**, 139 (2018).
3. Y. Li, J.-T. Han, C.-A. Wang, H. Xie, and J. B. Goodenough, *J. Mater. Chem.*, **22**, 15357 (2012).
4. D. Rettenwander, A. Welzl, S. Pristat, F. Tietz, S. Taibl, G. J. Redhammer, and J. Fleig, *J. Mater. Chem. A*, **4**, 1506 (2016).
5. M. A. Kraft, S. P. Culver, M. Calderon, F. Böcher, T. Krauskopf, A. Senyshyn, C. Dietrich, A. Zevalkink, J. Janek, and W. G. Zeier, *JACS*, **139**, 10909 (2017).
6. Y. Sun, K. Suzuki, K. Hara, S. Hori, T.-A. Yano, M. Hara, M. Hirayama, and R. Kanno, *J. Power Sources*, **324**, 798 (2016).
7. Y. Kato, S. Hori, T. Saito, K. Suzuki, M. Hirayama, A. Mitsui, M. Yonemura, H. Iba, and R. Kanno, *Nat. Energy*, **1**, 16030EP (2016).
8. H. Fang, S. Wang, J. Liu, Q. Sun, and P. Jena, *J. Mater. Chem. A*, **5**, 13373 (2017).
9. M. H. Braga, J. A. Ferreira, A. J. Murchison, and J. B. Goodenough, *J. Electrochem. Soc.*, **164**, A207 (2017).
10. S. Wang, L. Ben, H. Li, and L. Chen, *Solid State Ionics*, **268**, 110 (2014).
11. S. Breuer, D. Prutsch, Q. Ma, V. Epp, F. Preishuber-Pflügl, F. Tietz, and M. Wilkening, *J. Mater. Chem. A*, **3**, 21343 (2015).
12. P. Heitjans and S. Indris, *J. Phys.: Condens. Matter.*, **15**, R1257 (2003).
13. H. Stöffler et al., *J. Phys. Chem. C*, **122**, 15954 (2018).
14. M. Haaks, S. W. Martin, and M. Vogel, *Phys. Rev. B*, **96**, 863 (2017).
15. K. Arbi, W. Bucheli, R. Jiménez, and J. Sanz, *J. Eur. Ceram. Soc.*, **35**, 1477 (2015).
16. W. E. Tenhaeff, E. Rangasamy, Y. Wang, A. P. Sokolov, J. Wolfenstine, J. Sakamoto, and N. J. Dudney, *Chemelectrochem*, **1**, 375 (2014).
17. P. A. R. D. Jayatilaka, M. A. K. L. Dissanayake, I. Albinsson, and B.-E. Mellander, *Electrochim. Acta*, **47**, 3257 (2002).
18. T. Salkus, A. Dindune, Z. Kanepė, J. Ronis, A. Určinskas, A. Kezionis, and A. Orliukas, *Solid State Ionics*, **178**, 1282 (2007).
19. M. Schneider, A. Roters, J. Schumacher, and R. Samsinger, *Glaskeramik mit ionenleitender Restglasphase und Verfahren zu ihrer Herstellung*, DE 10 2018 102 387 B3 (2019).

20. M. Schneider, O. Hochrein, W. Schmidbauer, and M. Kunze, *Ionleitende Glaskeramik mit granatartiger Kristallstruktur, Verfahren zur Herstellung und Verwendung einer solchen Glaskeramik*, DE 10 2014 100 684 B4 2017.05.11 (2015).
21. F. Shen, M. B. Dixit, X. Xiao, and K. B. Hatzell, *ACS Energy Lett.*, **3**, 1056 (2018).
22. R. Böhmer, M. Maglione, P. Lunkenheimer, and A. Loidl, *J. Appl. Phys.*, **65**, 901 (1989).
23. A. Wiens, C. Kohler, M. Hansli, M. Schuessler, M. Jost, H. Maune, J. R. Binder, and R. Jakoby, *J. Eur. Ceram. Soc.*, **37**, 1487 (2017).
24. K. Waetzig, A. Rost, U. Langklotz, B. Matthey, and J. Schilm, *J. Eur. Ceram. Soc.*, **36**, 1995 (2016).
25. C.-L. Tsai, V. Roddatis, C. V. Chandran, Q. Ma, S. Uhlenbruck, M. Bram, P. Heitjans, and O. Guillon, *ACS Applied Materials & Interfaces*, **8**, 10617 (2016).
26. G. J. Brug, A. L. G. van den Eeden, M. Sluyters-Rehbach, and J. H. Sluyters, *J. Electroanal. Chem. Interfacial Electrochem.*, **176**, 275 (1984).
27. J. T. S. Irvine, D. C. Sinclair, and A. R. West, *Adv. Mater.*, **2**, 132 (1990).
28. A. Wachter-Welzl et al., *Solid State Ionics*, **319**, 203 (2018).
29. M. Gellert, K. I. Gries, C. Yada, F. Rosciano, K. Volz, and B. Roling, *J. Phys. Chem. C*, **116**, 22675 (2012).
30. S. D. Jackman and R. A. Cutler, *J. Power Sources*, **218**, 65 (2012).
31. D. O. Shin, K. Oh, K. M. Kim, K.-Y. Park, B. Lee, Y.-G. Lee, and K. Kang, *Sci. Rep.*, **5**, 18053EP - (2015).
32. Y. Zhang, F. Chen, R. Tu, Q. Shen, and L. Zhang, *J. Power Sources*, **268**, 960 (2014).
33. V. Thangadurai, S. Narayanan, and D. Pinzar, *Chem. Soc. Rev.*, **43**, 4714 (2014).
34. J. Fleig and J. Maier, *J. Am. Ceram. Soc.*, **82**, 3485 (1999).
35. D. Rettenwander, A. Welzl, L. Cheng, J. Fleig, M. Musso, E. Suard, M. M. Doeff, G. J. Redhammer, and G. Amthauer, *Inorg. Chem.*, **54**, 10440 (2015).
36. N. J. J. de Klerk and M. Wagemaker, *ACS Appl. Energy Mater.*, **1**, 5609 (2018).